

Laser printing of silver and silver oxide

Jordan M. Adams^{1*}, Daniel Heligman¹, Ryan O'Dell¹, Christine Y. Wang¹, and Daniel Young²

¹Riverside Research Institute, 2640 Hibiscus Way, Beavercreek, OH 45431 ²Wright State University, 3640 Colonel Glenn Hwy, Dayton, OH 45435

*Corresponding author: jadams@riversideresearch.org

We show that direct laser writing (DLW) in aqueous silver nitrate with a 1030 nm femtosecond (fs) laser results in deposition of a mixture of silver oxide and silver, in contrast to the pure silver deposition previously reported with 780 nm fs DLW. However, adding photoinitiator prevents silver oxide formation in a concentration-dependent manner. As a result, the resistivity of the material can also be controlled by photoinitiator concentration with resistivity being reduced from approximately $9e-3 \Omega m$ to $3e-7 \Omega m$. Silver oxide peaks dominate the X-ray diffraction spectra when no photoinitiator is present, while the peaks disappear with photoinitiator concentrations above 0.05wt%. While femtosecond pulses are needed to initiate deposition, a continuous-wave laser when well overlapped with the previously written material and supplying enough average power can lead to further printing, suggesting thermal deposition can also occur where the photoinitiator molecule also acts as a general reducing agent that prevents oxide formation. We also compare the surface quality of printed lines for different photoinitiator concentrations and laser printing conditions. A THz polarizer and metamaterial are printed as a demonstration of silver oxide printing.

Keywords: laser, femtosecond, silver, direct-laser-writing

1. Introduction

Multiphoton fabrication of metals is an additive manufacturing technique capable of printing high-reduction potential metals such as gold, platinum, palladium, or silver [1-11]. Typically, an 800 nm femtosecond laser is used to excite a photoinitiator with absorption around the two-photon wavelength of 400 nm, which then reduces dissolved metal ions [2-7]. Deposition may occur by the neutral atoms growing into nanoparticles that then aggregate onto the substrate [3,4].

While early work focused on the direct writing of metal from polymeric or sol-gel precursors [12,13], more recent work has focused on fabrication in liquid environments. The first demonstration used an 800 nm femtosecond laser to print silver out of aqueous silver nitrate with no photoinitiator and achieved a resistivity value of 3.3 times that of the bulk silver value of $1.59e-8 \Omega m$ [1]. Following works added photoinitiators [2] and surfactants [3] to the precursor to decrease the linewidth <200 nm. A 1030 nm femtosecond laser has also been used to print silver from a photoinitiator/surfactant precursor and achieved similar linewidths [8].

While there is ample literature on the multiphoton printing of metals, the reported electrical conductance data and phase characterization is sparse. There are outstanding research questions regarding the phase of grown materials, especially when no photoinitiator is present and the deposition may be partially thermally induced [1, 2]. Besides this, there are no reports of other silver compounds being printed, such as silver-oxide.

Here, we report on the fabrication of silver/silver-oxide using an aqueous $AgNO_3$ precursor solution containing varying amounts of photoinitiator precursor. Unlike the majority of reports which used a ~ 800 nm femtosecond laser, we use a 1030 nm femtosecond laser and PI369 photoinitiator for 3-photon reduction. At 1030 nm with low photoinitiator concentrations, we show evidence that the printed structures are mixed metal/oxide with poor conductivity. Higher photoinitiator concentration results in pure metal deposition and a conductivity close to bulk silver. Additionally, EDS cross sections reveal the glass substrate is partially melted and mixed into the printed films only when no photoinitiator is present, further corroborating the transition from low-melting temperature silver oxide to silver. From here, we find high PI% leads to lines with fewer holes and less variability in width. Additionally, we also find varying pulse energy and scan speed can transition lines from crystalline to smooth, even without surfactants. Finally, we show two THz devices, a polarizer with variable line spacing that has an extinction ratio >750 and a split-ring resonator (SRR) array with fundamental resonance just below 0.4 THz. We believe this study offers valuable insight into maximizing conductivity of laser printed silver by preventing silver oxide when unwanted. Additionally, this study shows that printing silver oxide is possible, which can be valuable for applications involving supercapacitors [14], catalyzing specific reactions [15], as well as applications requiring specific bandgap properties [16].

2. Methods

An aqueous solutions of silver nitrate with a 1:1 mass ratio was prepared as the base precursor. Photoinitiator PI-369 (2-Benzyl-2-(dimethylamino)-1-[4-(4-morpholinyl)phenyl]-1-butanone) was added at concentrations between 0 wt% to 0.37 wt%, where the solution was fully saturated. A drop of the solution was placed on a borosilicate cover slip and a 1030 nm Yb-fiber femtosecond laser (~ 200 fs, 20 MHz) focused by 1.3 NA oil immersion objective was used to directly deposit material on the cover slip.

3. Results

Phase analysis was performed using X-ray diffraction (XRD) to determine the relative amounts of silver oxide and metallic silver. For these measurements, films were written in a raster pattern to provide sufficient material for analysis. The laser power was 600 mW with a scan velocity of 0.5 mm/s and raster steps of 1 μm . Figure 1 (a) shows the X-Ray Diffraction (XRD) results. The top line shows the XRD peak from the 0% photoinitiator (PI) sample is predominately [1 3 2] AgO ($\text{Ag}^{\text{I}}\text{Ag}^{\text{III}}\text{O}_2$) [17], with traces of metallic silver. At 0.01% PI the main peak becomes either AgO [1 2 1] or Ag_2O [1 1 1], which have overlapping peaks. In both 0 and 0.01% PI samples, pure silver peaks are evident but still relatively small. At 0.05% PI concentration, the primary phase is pure silver, and the silver oxide peaks are relatively small. Finally, at 0.1% PI there are no noticeable silver oxide peaks remaining. The fraction of area under the two oxide peaks to the total area of the combined peaks is plotted in Figure 1 (b) for each concentration, which qualitatively shows amount of oxide being reduced with increasing concentration.

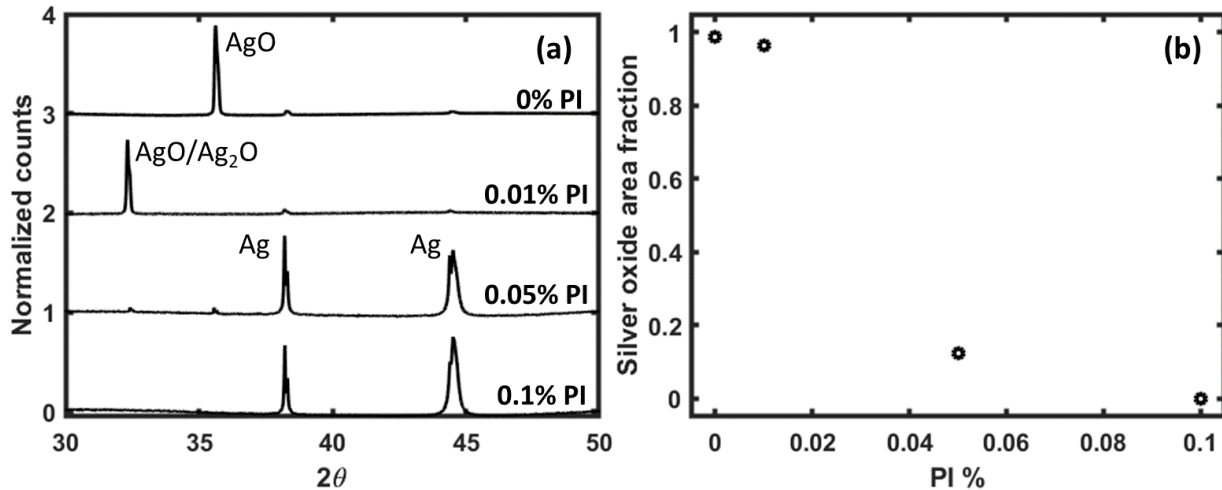


Fig. 1. (a) Normalized X-Ray Diffraction (XRD) measurements for each sample. (b) The fraction of area under the silver oxide peaks to the total area of the combined silver and silver oxide peaks.

In order to study material resistivity as a function of PI concentration, a Versalabs PPMS 4-point probe measurement system was used to measure the resistance. In addition to the films used for XRD analyses, single lines were printed between silver-paste electrode pads, utilizing a laser power of 100 mW power and 3 $\mu\text{m}/\text{s}$ scan speed. The resistivity versus PI concentration for both lines and pads is shown in Figure 2. SEM imaging (JEOL 7900 FLV) was also used to approximate line geometry for estimating the resistivity. There is variation in the linewidth, w , and height, h , across the length of the line, L , which complicate the resistivity calculation. We assume a circular cross section for lines and calculate the resistivity, $\rho = R \frac{A}{L} = R \frac{\pi w^2}{4L}$, for the maximum and minimum linewidth, and plot the range of values with error bars on the plot. For films, the resistivity is $\rho = R \frac{wh}{L}$, where we use the respective height variation of the lines to plot a range of values with error bars. While previous reported work used a half-ellipse estimation for area of lines, which gives a lower resistivity [1], we found most lines and films are in fact partially buried in the glass with lines not being a half-circle or ellipse lying flat on the substrate. As a reference, the resistivity of bulk silver oxide is $5.4e - 4 \Omega\text{m}$ [18] and bulk metallic silver is $1.58e - 8 \Omega\text{m}$ where both are plotted in Figure (2) as the thick upper and lower dashed lines, respectively. For the 0 wt% PI concentration mean resistivity of the large film was $8.8e-3 \text{ Wm}$, while the mean value for individual line was $1.3e - 3 \Omega\text{m}$. With increasing PI concentration, the mean resistivity of the films drops to $2.8e - 7 \Omega\text{m}$, $\sim 18\text{x}$ that of bulk silver while the line resistivity drops to only $3.5e-6$, possibly due to poor connections at the electrodes. The decrease in resistivity with PI concentration is consistent with a shift from a silver oxide phase to a mixed metal/oxide, and finally to a pure metallic phase. PI 0.1 wt% is sufficient to achieve minimum line resistivity, while a significantly higher concentration of 0.37% PI achieved a similar resistivity value for the films. Besides film porosity, this may be due to a small amount of oxide on the surface of individual lines that make up the film, degrading the bulk resistivity.

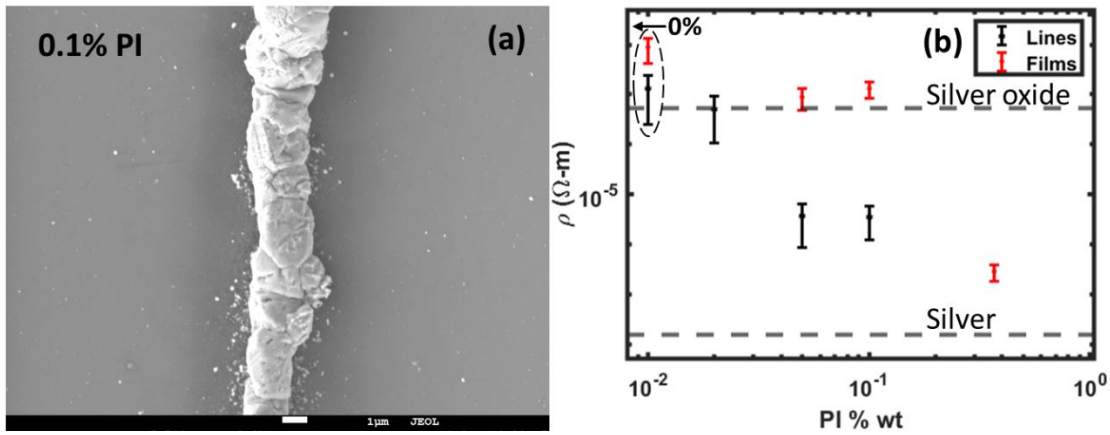


Fig. 2: (a) Line written at 100 mW with 3 μm/s scan speed and (b) calculated resistivity as a function of PI concentration for individual lines and films written in a raster pattern.

Secondary-electron SEM images of the raster pattern films are shown in Figure 3, for 0% PI and 0.37% PI. In the 0% PI sample (Figure 3 (a)), the film has evidence of discrete pores and some cracking, while overlaid with crystallites. In the top inset, the optical image clearly shows the front side is brown colored which matches silver oxide, while some regions are also covered in highly reflective silver crystallites. The back side of the film, which is attached to the glass, is a lighter mahogany color, which may be from silver diffusing into the borosilicate substrate [19]. The 0.37% PI sample shows no porosity or cracking evident along with the overlaid crystallites. In this case, the optical image shows a grey film with matches silver, while the back side is the same light mahogany color as the 0% PI sample. Figure 3 (d)-(f) show an EDS map of a crystallite and the film for a sample printed with no photoinitiator. While the crystallites are pure silver based on the EDS measurements, the films have varying concentrations of silicon and oxygen. The resistivity data is likely insensitive to the phase of the crystallites since they do not form a continuous electrical pathway. At the same time, we found EDS results for the 0.37% sample were similar, with silicon and oxygen present inside the film. As the electron beam could be interacting with the substrate in the film region, it is inconclusive whether oxygen and silicon are actually present inside the films.

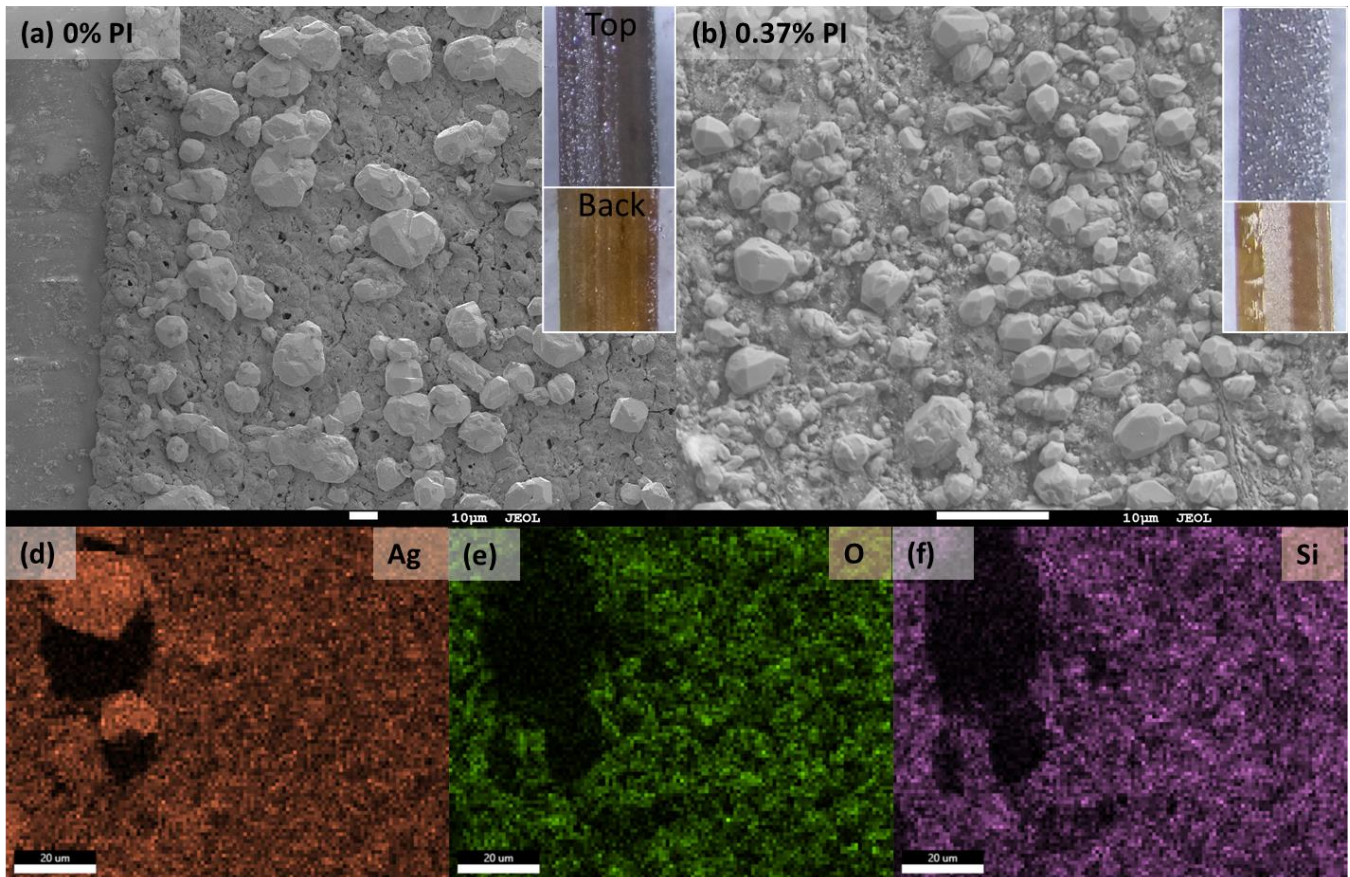


Fig. 3: SEM images of bulk films for (a) a 0 wt% PI sample and (b) a 0.37 wt% PI sample with insets showing optical images of the front and back side of the films. (d) Silver, (e) oxygen, and (d) silicon EDS maps of a small region of a 0% PI film with a crystallite.

To separate the substrate signal from the film signal, we performed EDS on cross sections show in Figure 4. Figure 4 (a)-(d) shows an SEM image of the cross-section of a 0% PI film as well as silver, oxygen, and silicon elemental maps. Certain regions of the film have high concentrations of both silicon and oxygen at the same locations, while silver is well distributed. This indicates the glass may be partially mixing within the film. On the other hand, Figure 4 (e)-(h) shows the results for a 0.37% PI cross section. In this case, the oxygen and silicon are confined to the glass and not mixed with the film. Since the film experienced no visible melting and mixing as before, this further corroborates the transition from low-melting temperature silver-oxide to pure silver with the addition of photoinitiator. Near the interface the glass itself does have small concentrations of silver (<1%), although too small to see in the EDS maps. This along with the bright Mahogany color on the back side of the films suggests silver atoms may diffuse into the substrate to locally form a silver borosilicate glass [19].

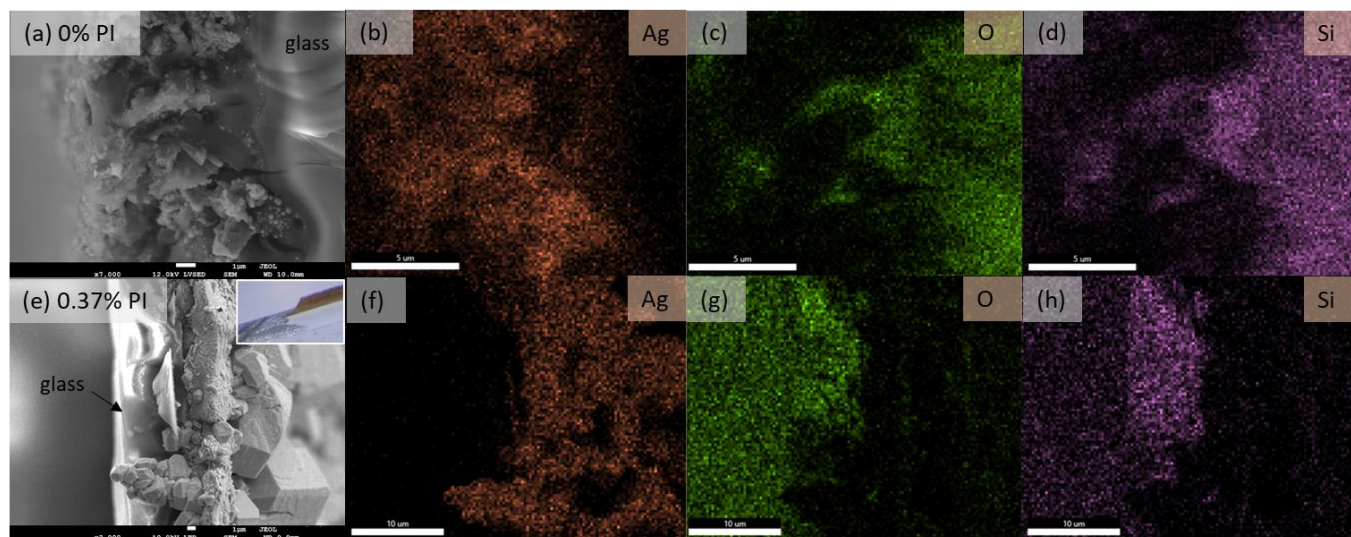


Fig. 4: SEM and EDS cross section images of films written from a (a)-(d) 0% PI solution and (e)-(h) 0.37% PI solution. (e) The 0.37% PI cross section was taken from a region that naturally broke away from the cover slip and curled, as shown in the optical inset.

Comparison of the EDS data, phase data, and resistivity data suggest that the material written from the 0% PI solution contain silver oxide while increasing the PI concentration reduces and ultimately eliminates oxide formation. The estimated resistivity values may be worse than bulk silver due to surface roughness, porosity, poor connection to the electrodes, and variability in cross section which makes an accurate calculation difficult. Adding surfactants will improve the printing quality [3] which will shift this data towards lower resistivity values and may also eliminate the crystallites resulting in a smoother film surface.

Small nanoparticles formed via photoreduction would experience little plasmonic absorption and laser-induced heating with the 1030 nm femtosecond laser [20], which could explain silver oxide forming. The low-temperature environment in the oxygen rich water could allow silver oxide growth on nanoparticles (NPs) as they slowly grow [21, 22] and eventually deposit on the glass. In contrast, an 800 nm laser would more strongly excite silver nanoparticles owing to the second harmonic of the fundamental wavelength overlapping the 400 nm plasmonic peak [20], keeping them at a higher temperature and leading to more rapid growth. The hotter temperature of the particles and reduced time for growth could prevent oxide formation.

Using a longer wavelength to excite higher-order multiphoton absorption, we needed at least 60 mW at 1030 nm for deposition to occur compared to <15mW at 800 nm [1]. The higher laser power does mean that there will be significantly more single photon absorption once the structure is fabricated. The films will reach higher temperatures, causing local melting and mixing of the substrate into the low-melting temperature silver oxide. Additionally, the higher temperature of the films may lead to growth of the crystallites via thermal reduction. While femtosecond pulses are at first needed to initiate the deposition, we found CW (continuous wave) illumination could continue deposition of films when the laser was well overlapped, such as in our experiment of printing films with 1 μ m raster steps. The films printed with CW light appeared to be visually similar in appearance to films printed using pulses for both with and without photoinitiator, although more study is needed for confirmation. This suggests that a significant part of the printing process may actually be thermally driven at this laser power when there is modest overlap of the laser with the previously written material. In this case, the photoinitiator can also act as a general reducing agent that is thermally or chemically activated.

After extended deposition time, we also found higher power CW illumination (> 1W) could sporadically initiate deposition on the bare glass substrate. It has been reported that CW illumination at wavelengths from visible to NIR can lead to silver nanoparticle deposition on borosilicate in a silver nitrate solution [23] which was attributed to Ag₂O readily forming on the unexposed surface. On top of this, we found that the glass surface becomes covered with particles during the fabrication process. This does not just occur near

the printing regions, but more generally where the solution touches the glass. Nanoparticles formed during printing that are not deposited into the printed structure may be suspended in the solution and later adhere to the substrate. The presence of these particles along with the naturally Ag₂O forming on the surface may help initiate deposition even under CW illumination.

4. Printing quality of lines

We investigated the printed line quality and found it varies with PI concentration as well as laser power and scan speed. Figure 5 (a) – (d) show lines written at 0%, 0.02%, 0.05% and 0.1% PI concentrations with 100 mW and 3 microns/s scan speed. The 0% and 0.02% PI lines had linewidths varying from ~2.5-8 microns in width, while the rest of the lines varied from ~1.5-4 microns. The 0% line have a melted appearance with large holes evident, matching the films. With higher PI%, the lines appear more crystalline, with fewer holes and lower variability in linewidth. Figure 4 (b) shows a line written at 0% PI, 60 mW, <3 $\mu\text{m/s}$, and with multiple passes of the laser. 60 mW was the threshold power for deposition, requiring multiple scans to form a continuous line. Unlike the previous lines, it is visibly entrenched into the glass and displays larger, discrete crystals. This lowest power may prevent melting as well as uncontrolled heating and growth of the line. The opposite case appears at fast scanning with higher power. Figure 4 (c) shows a smooth line written with 0% PI, 600 mW, and 20 mm/s. Multiphoton metal prints shown in the literature appear to have high surface roughness compared to polymer printing. Unlike typical photopolymers, metals are highly absorbing at the fundamental laser frequency. Heating the metal would lead to continuous thermal reduction and growth, while ions are continually diffusing toward the surface. This thermal reduction, which depends on the random motion of ions, may contribute to high surface roughness. However, even before the bulk metal is formed, the initially formed nanoparticles would scatter the light [24] leading to a highly distorted and dynamically changing focus during the process of the nanoparticles aggregating and depositing on the substrate [3]. The scattering at the focus could result in high surface roughness, such as in Laser-Induced Periodic Surface Structures [25]. Using higher pulse energy and scanning faster to reduce the exposure time would limit the extent of this dynamic scattering as well as thermal reduction. The diffusion time of silver ions in water at room temperature across a $\sim 1 \mu\text{m}^2$ voxel region would be $\sim 6 \mu\text{s}$ [26], while the diffusion time of metal NPs could $\sim 600 \mu\text{s}$ [27] to $\sim 10 \text{ms}$ [28]. The laser exposure time in the voxel region with 5 $\mu\text{m/s}$ and 20 mm/s scanning would be 0.2 seconds and 50 μs , respectively. For fast scanning, the laser exits the voxel region before significant ion diffusion can occur resulting in less thermal reduction and reduced random surface growth. Additionally, the laser focus over the entire exposure would be more uniform and stable with time, since NPs would be relatively stagnant and likely wouldn't have grown as large.

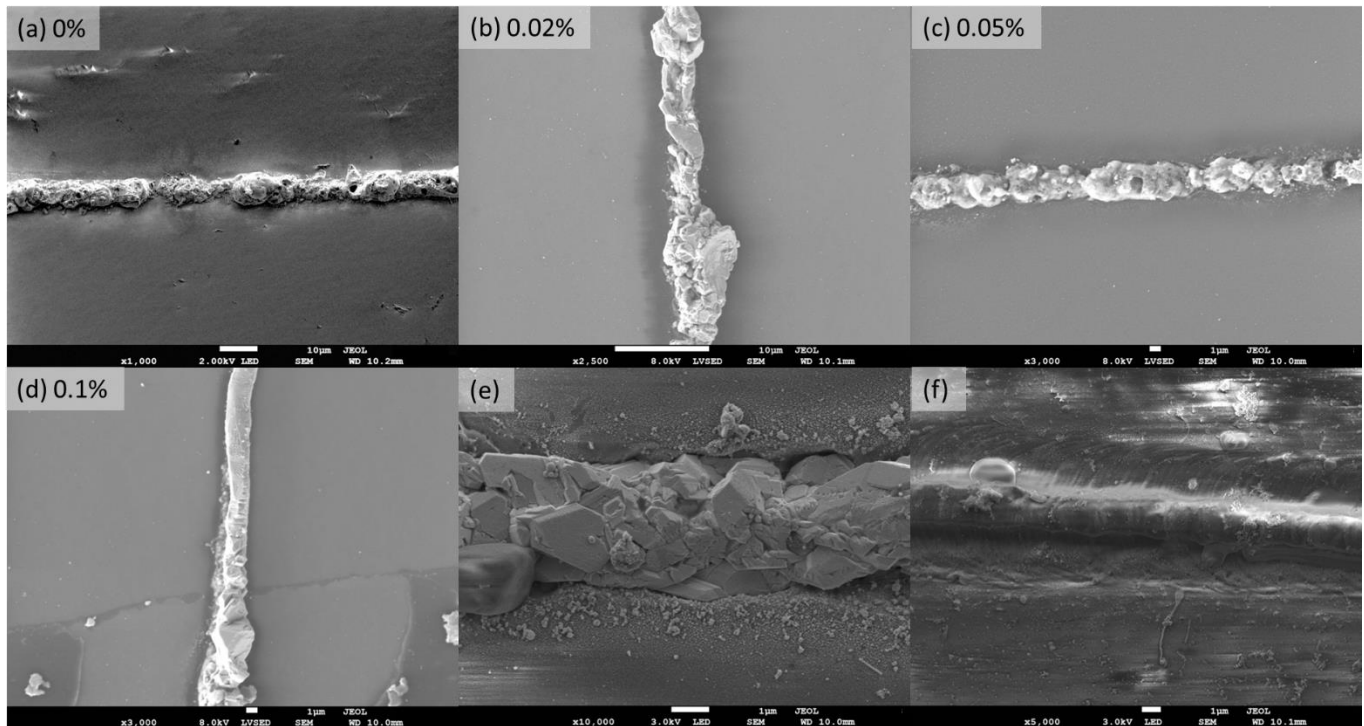


Fig. 5: Line printing conditions are: (a) 0%, (b) 0.02%, (c) 0.05%, and (d) 0.1% PI at 100 mW and 3 $\mu\text{m/s}$. (e) 0% PI, 60 mW, <5 $\mu\text{m/s}$ and (f) 0% PI, 600 mW, 30 mm/s.

5. THz devices

In order to demonstrate silver oxide THz devices, we fabricated structures using the 0%PI aqueous silver nitrate solution. While the resistivity is several orders higher than that pure silver, it is still low enough to have strong absorption and reflection in the THz band.

The TeraMetrix THz Time-Domain Spectrometer was used to characterize the signal. For the first device, a polarizer was fabricated at different line spacings. The resulting perpendicular and parallel polarization reflections are shown in Figure 6 (a) and (b) with the line spacings of 300 μm , 200 μm , 50 μm , and 25 μm shown as an inset with respective labels from 1 through 5. Figure 6 (c) shows an average cross-section for both polarizations and the corresponding extinction ratio which is the parallel divided by the perpendicular polarization reflection. While the perpendicular polarization is mostly transmitted with spacings of 50 microns and higher, the parallel component is significantly reflected. 50 μm spacing gave the best extinction ratio of >750 , while the lines began to behave as a normal mirror at line spacings down to 25 μm .

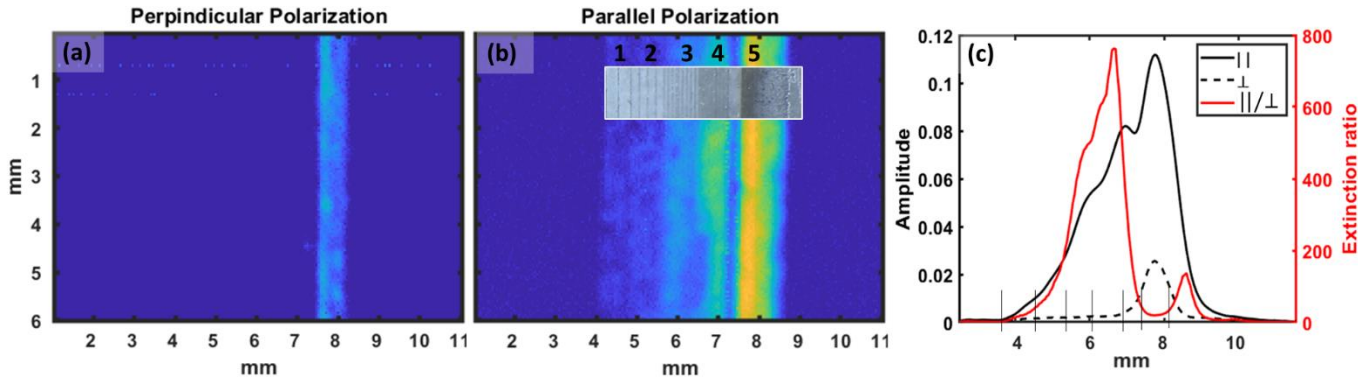


Fig. 6: (a), (b) Perpendicular and parallel polarization reflections from the polarizer. Inset on (b) is an optical image showing the black-brown lines at different spacings written on the coverslip. (c) Average cross-section reflection for both polarizations and the corresponding extinction ratio.

Next, we printed an electromagnetic split ring resonator (SRR) metamaterial array. Metamaterials have bulk optical properties dependent on the geometry of the unit cell [29]. The SRR metastructure can be viewed as an LC resonator in terms of an equivalent circuit model. The parametric length of the stripline, the dimensions of capacitive gap and the permeability/permittivity of ambient material dictate the structure's resonant frequency. Tuning this frequency will allow for changing the bulk metamaterial's optical properties [30, 31]. Figure 7 (a) shows an SEM image of one part of the SRR array. The length of each side is 100 microns, for a total length of 300 microns. Since the substrate is 180 μm , there are Fabry-Perot resonances that overlap with the SRR resonances. Instead of showing the standard reflectivity, we divide the raw reflection spectrum by the reflection from the bare glass cover slip to eliminate the substrate interference resonances. Figure 7 (b) shows the results of the SRR array for both simulation and experiment, where we found using a simulation glass index $n \sim 2.4$ gives the best overlap. This $n \sim 2.4$ was found to match the THz index of $x = 20$ sodium borosilicate glass $((x)Na_2O20B_2O_3(80 - x)SiO_2)$ [33].

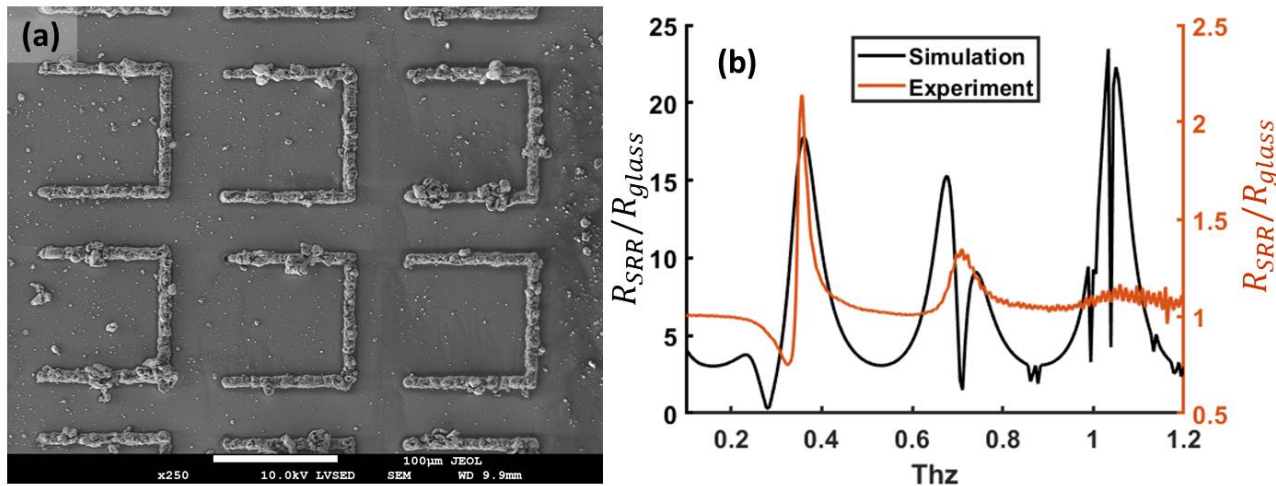


Fig. 7: (a) SEM image Split ring resonator (SRR) array unit cells. (b) Simulated and experimental reflection response from the SRR array.

6. Conclusion

In conclusion, we demonstrated that the amount of oxide in silver structures fabricated by DLW from aqueous silver nitrate solutions can be controlled by the PI concentration across a wide range when using a 1030 nm femtosecond laser. The resistivity of printed

structures is controlled by photoinitiator concentration from approximately $9e-3 \Omega m$ to $3e-7 \Omega m$. X-ray diffraction results show that silver oxide dominates the microstructure when no photoinitiator is present. Increasing concentrations of photoinitiator result in an increasing presence of metallic silver. The photoinitiator and the laser printing condition have a large effect on the surface of the line. A THz polarizer and metamaterial are shown as a demonstration of silver oxide printing. While further understanding of these growth mechanisms will be required to achieve the fabrication of optimized geometries, we show that careful control of PI concentration could allow precise fabrication of structures consisting of mixed metal/oxide materials.

Research funding: This work was supported with internal funding from Riverside Research Institute and Wright State University

Author contribution: J.A. performed experiments and analysis. R.O. performed resistivity measurements. D.H. performed THz SRR design and simulation. C.W. advised the project. D.Y. advised the project and performed XRD and EDS measurements. All authors have accepted responsibility for the entire content of this manuscript and approved its submission.

Conflict of interest: Authors state no conflict of interest.

Data availability statement: The data that supports the finding of the current study are available from the corresponding author upon reasonable request.

References

1. T. Tanaka, A. Ishikawa and S. Kawata, "Two-photon-induced reduction of metal ions for fabricating three-dimensional electrically conductive metallic microstructure", *Appl. Phys. Lett.*, vol. 88, no. 8, pp. 081107, 2006.
2. A. Ishikawa, T. Tanaka, and S. Kawata, "Improvement in the reduction of silver ions in aqueous solution using two-photon sensitive dye," *Applied Physics Letters*, vol. 89, no. 11, pp. 113102, 2006.
3. Y.Y. Cao, N. Takeyasu, T. Tanaka, X.M. Duan, and S. Kawata, "3D Metallic Nanostructure Fabrication by Surfactant-Assisted Multiphoton-Induced Reduction," *Small*, vol. 5, no. 10, pp. 1144-1148, 2009.
4. Y.Y. Cao, X.Z. Dong, N. Takeyasu, T. Tanaka, Z.S. Zhao, X.M. Duan, and S. Kawata, "Morphology and size dependence of silver microstructures in fatty salts-assisted multiphoton photoreduction microfabrication," *Applied Physics A*, vol. 96, no. 2, pp. 453-458, 2009.
5. W.E. Lu, et. al., "Femtosecond direct laser writing of gold nanostructures by ionic liquid assisted multiphoton photoreduction," *Opt. Mater. Express*, vol. 3, no.10, pp.1660-1673, 2013.
6. W. Jin, M.L. Zheng, Y.Y. Cao, X.Z. Dong, Z.S. Zhao, and X.M. Duan, "Morphology Modification of Silver Microstructures Fabricated by Multiphoton Photoreduction," *Journal Of Nanoscience And Nanotechnology*, vol. 11, no.10, pp. 8556-60, 2011.
7. L. D. Zarzar, B. S. Swartzentruber, J. C. Harper, D. R. Dunphy, C. J. Brinker, J. Aizenberg, and B. Kaehr, "Multiphoton Lithography of Nanocrystalline Platinum and Palladium for Site-Specific Catalysis in 3D Microenvironments," *J. Am. Chem. Soc.*, vol. 134, pp. 4007-4010, 2012.
8. L. Liu, D. Yang, W. Wan, H. Yang, Q. Gong, and Y. Li, "Fast fabrication of silver helical metamaterial with single-exposure femtosecond laser photoreduction," *Nanophotonics*, vol. 8, no. 6, pp. 1087-1093, 2019.
9. B.B. Xu , et al, "Flexible nanowiring of metal on nonplanar substrates by femtosecond-laser-induced electroless plating," *Small*, vol. 6, no. 16, pp. 1762-1766, 2010.
10. M.R. Lee, et al., "Direct metal writing and precise positioning of gold nanoparticles within microfluidic channels for SERS sensing of gaseous analytes," *ACS Applied Materials & Interfaces*, vol. 9, no. 45, pp. 39584-39593, 2017.
11. J. Jones, M. Snowdon, S. Rathod, P. Peng, "Direct laser writing of copper and copper oxide structures on plastic substrates for memristor devices," *Flexible Printed Electronics*, vol. 8, no. 1, pp. 015008, 2003.
12. K. Kaneko, H.B. Sun, X.M. Duan, and S. Kawata, "Two-photon photoreduction of metallic nanoparticle gratings in a polymer matrix," *Applied Physics Letters*, vol. 83, no. 7, pp.1426-1428, 2003.
13. T. Baldacchini, A.C. Pons, J. Pons, C.N. LaFratta, J.T. Fourkas, Y. Sun, and M.J. Naughton, "Multiphoton laser direct writing of two-dimensional silver structures," *Optics Express*, vol. 13, no. 4, pp. 1275-1280, 2005.

14. M. Mirzaeian, A.A. Ogwu, H.F. Jirandehi, S. Aidarova, Z. Ospanova, and N. Tsendzughul, "Surface characteristics of silver oxide thin film electrodes for supercapacitor applications. Colloids and Surfaces," *A: Physicochemical and Engineering Aspects*, vol. 519, pp.223-230, 2017
15. M.F. Fellah, R.A. van Santen, and I. Onal, "Epoxidation of ethylene by silver oxide (Ag₂O) cluster: A density functional theory study," *Catalysis Letters*, vol. 141, pp.762-771, 2011.
16. W. Jiang, X. Wang, Z. Wu, X. Yue, S. Yuan, H. Lu, and B. Liang, "Silver oxide as superb and stable photocatalyst under visible and near-infrared light irradiation and its photocatalytic mechanism," *Industrial & Engineering Chemistry Research*, vol. 54, no. 3, pp. 832-841, 2015.
17. N.K. Abdalameer, K.A. Khalaph, and E.M. Ali, "Ag/AgO nanoparticles: Green synthesis and investigation of their bacterial inhibition effects," *Materials Today: Proceedings*, vol. 45, pp. 5788-5792, 2021.
18. P.N. Reddy, M. Reddy, J.F. Pierson, and S. Uthanna, "Characterization of silver oxide films formed by reactive RF sputtering at different substrate temperatures," *International Scholarly Research Notices*, 2014.
19. J.L. Piguet and J.E. Shelby. "Preparation and properties of silver borate glasses," *Journal of the American Ceramic Society*, vol. 68, no. 8, pp. 450-455, 1985.
20. A. Singh, S. Jha, G. Srivastava, P. Sarkar, and P. Gogoi, "Silver nanoparticles as fluorescent probes: new approach for bioimaging," *Int. J. Sci. Technol. Res*, vol. 2, no. 11, pp.153-157, 2013.
21. N. Grillet, et. al., "Photo-oxidation of individual silver nanoparticles: a real-time tracking of optical and morphological changes," *The Journal of Physical Chemistry C*, vol. 117, no. 5, pp.2274-2282, 2013.
22. V. Sundaresan, J.W. Monaghan, and K.A. Willets, "Visualizing the effect of partial oxide formation on single silver nanoparticle electrodisolution," *The Journal of Physical Chemistry C*, vol. 122, no. 5, pp. 3138-3145, 2018.
23. K. Setoura, S. Ito, M. Yamada, H. Yamauchi, and U. Miyasaka, "Fabrication of silver nanoparticles from silver salt aqueous solution at water-glass interface by visible CW laser irradiation without reducing reagents," *Journal of Photochemistry and Photobiology A: Chemistry*, vol. 344, pp. 168-177, 2017.
24. S.K. Eah, H.M. Jaeger, N.F. Scherer, G.P. Wiederrecht, and X.M. Lin, "Scattered light interference from a single metal nanoparticle and its mirror image," *The Journal of Physical Chemistry B*, vol. 109, no. 24, pp. 11858-11861, 2005.
25. J. Bonse, S.V. Kirner, and J. Krüger, "Laser-induced periodic surface structures (LIPSS)," *Handbook of laser micro-and nano-engineering*, pp.1-59, 2020.
26. P. Vanysek, "Ionic conductivity and diffusion at infinite dilution," *CRC hand book of chemistry and physics*, pp. 5-92, 1993.
27. K. Wong, C. Chen, K. Wei, V.A.L Roy, and S.M. Chathoth, "Diffusion of gold nanoparticles in toluene and water as seen by dynamic light scattering," *Journal of Nanoparticle Research*, vol. 17, pp.1-8, 2015.
28. F. Giorgi, et. al., "The influence of inter-particle forces on diffusion at the nanoscale," *Scientific reports*, vol. 9, no. 1, pp. 12689, 2019.
29. D.R. Smith, J.B. Pendry, and M.C.K. Wiltshire, "Metamaterials and negative refractive index," *Science*, vol. 305, no. 5685, pp. 788-792, 2004.
30. D.M. Heligman, A.M. Potts, R.V. Aguilar, "Numerical simulation of split ring resonator near-fields and antiferromagnetic magnon hybridization," *Optical Materials Express*, vol. 14, no. 3, pp. 687-695, 2024.
31. JD Baena, et al. "Equivalent-circuit models for split-ring resonators and complementary split-ring resonators coupled to planar transmission lines," *IEEE Transactions On Microwave Theory And Techniques*, vol. 53, no. 4, pp. 1451-1461, 2005.
32. M. Naftaly and A. Gregory, "Terahertz and microwave optical properties of single-crystal quartz and vitreous silica and the behavior of the boson peak," *Applied Sciences*, vol. 11, no. 15, pp. 6733, 2021.
33. N.J. Tostanoski, and S.K. Sundaram, Visible-Terahertz Refractive Indices Correlation in Sodium Borosilicate Glasses. *Journal of Infrared, Millimeter, and Terahertz Waves*, vol. 44 no. 1, pp. 17-36, 2023.

